communications physics

Article

https://doi.org/10.1038/s42005-024-01857-6

Unveiling nodeless unconventional superconductivity proximate to honeycomb-vacancy ordering in the Ir-Sb binary system

Check for updates

V. Sazgari[1], T. P. Ying[2,3], J. N. Graham[1], C. Mielke III[1], D. Das[1], S. S. Islam[1], S. Shin[1], M. Medarde[1], M. Bartkowiak[1], R. Khasanov[1], H. Luetkens[1], H. Hosono[2] & Z. Guguchia[1]

Vacancies in solid-state physics are underexplored in materials with strong electron-electron correlations. Recent research on the Ir-Sb binary system revealed an extended buckled-honeycomb vacancy (BHV) order. Superconductivity arises by suppressing BHV ordering through high-pressure growth with excess Ir atoms or Rh substitution, yet the superconducting pairing nature remains unknown. To explore this, we conducted muon spin rotation experiments on $Ir_{1-\delta}Sb$ (synthesized at 5.5 GPa, $T_c = 4.2$ K) and ambient pressure synthesized optimally Rh-doped $Ir_{1-x}Rh_xSb$ (x=0.3, $T_c = 2.7$ K). The exponential temperature dependence of the superfluid density suggests a fully gapped superconducting state exists in both samples. The ratio of T_c to the superfluid density resembles that of unconventional superconductors. A significant increase in the superfluid density in the high-pressure synthesized sample correlates with T_c, indicating that unconventional superconductivity is intrinsic to the Ir-Sb binary system. These findings, along with the dome-shaped phase diagram, highlight IrSb as the first unconventional superconducting parent phase with ordered vacancies, requiring further theoretical investigations.

Vacancies and defects play crucial roles in the properties of materials, and their significance is evident in various classes of materials, including transition metal dichalcogenides (TMDs)[1–5], Fe-based superconductors[6–9] and cuprate high-temperature superconductors[10–12]. In transition metal dichalcogenides like MoS_2 or WSe_2, vacancies and defects can significantly influence electronic and optical properties[1]. For instance, point defects such as sulfur or selenium vacancies can introduce localized states into the band gap, affecting the materials conductivity and optical absorption. Defects can serve as active sites for chemical reactions and play a role in catalysis[2]. Defects in TMDs can also induce magnetism and lead to interesting magnetic properties[3–5].

Several studies have investigated the impact of vacancy ordering in different iron-based superconductors[6,7]. For example, in iron chalcogenide superconductors such as FeSe, the ordering of selenium vacancies has been observed to influence the electronic structure and can lead to novel phenomena, including the emergence of superconductivity[8]. Understanding and controlling the role that vacancies and defects play in materials is therefore essential for tailoring their properties for specific applications. Researchers often explore the effects of defects to harness their potential benefits or mitigate undesirable consequences in various materials systems, ranging from electronics and catalysis to energy storage and superconductivity.

In this context, scientists have uncovered a distinct type of vacancy ordering in the Ir-Sb binary system $Ir_{16}Sb_{18}$, manifesting as an extended buckled-honeycomb vacancy (BHV) order[13,14]. The system $Ir_{16}Sb_{18}$ has been identified as the first superconducting parent phase known to exhibit ordered vacancies. The emergence of superconductivity in Ir-Sb is closely linked to the suppression of the BHV ordering. This suppression is achieved through two distinct methods: high-pressure growth of $Ir_{1-\delta}Sb$ involving the squeezing of additional Ir atoms into the vacancies, and isovalent Rh substitution $Ir_{1-x}Rh_xSb$. These interventions disrupt the ordered vacancy structure, paving the way for superconductivity. However, while the connection between vacancy ordering and superconductivity is established, the exact nature of the superconducting

[1]PSI Center for Neutron and Muon Sciences CNM, 5232 Villigen PSI, Switzerland. [2]MDX Research Center for Element Strategy, Institute of Science Tokyo, Yokohama, 226-8503, Japan. [3]Beijing National Laboratory for Condensed Matter Physics, Institute of Physics, Chinese Academy of Sciences, 100190 Beijing, China. e-mail: zurab.guguchia@psi.ch

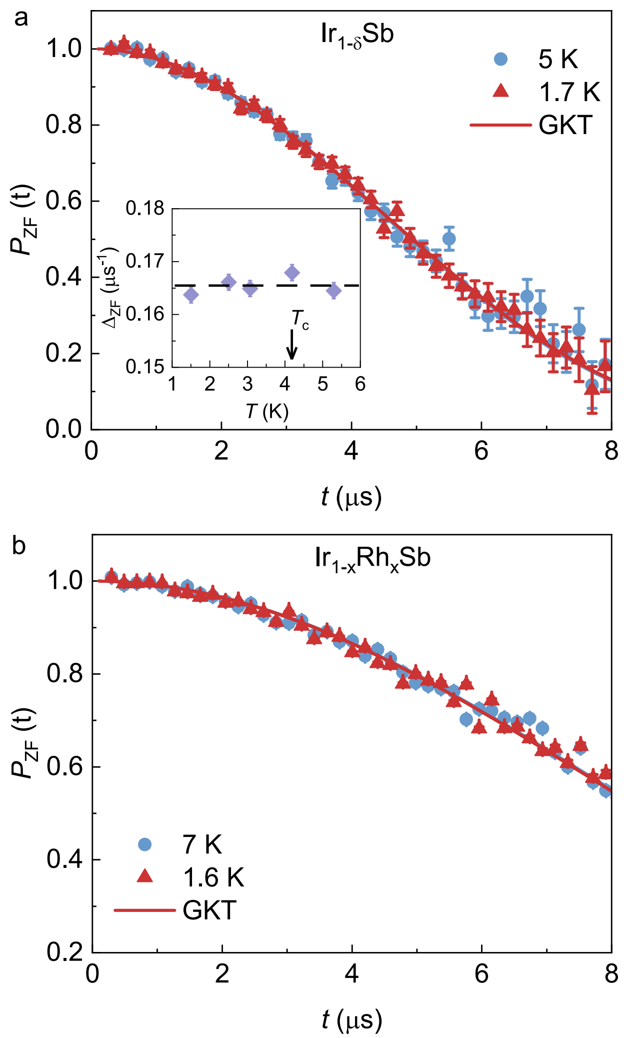

Fig. 1 | Zero-field (ZF) μSR time spectra. Time evolution of zero-field muon spin polarization $P_{ZF}(t) = A_{ZF}^{GKT}(t)/A_0$, measured above and below T_c for $Ir_{1-\delta}Sb$ (**a**), synthesized at 5.5 GPa and for $Ir_{1-x}Rh_xSb$ with $x = 0.3$ (**b**). Error bars are the standard error of means (s.e.m.) in about 10^6 events. The error of each bin count n is given by the standard deviation (s.d.) of n. The errors of each bin in $P_{ZF}(t)$ are then calculated by standard error (s.e.) propagation. The solid lines represent fits to the data by means of equation (1). The inset in panel **a** displays the temperature dependence of the zero-field muon spin relaxation rate Δ_{ZF} across $T_c \simeq 4.0$ K.

pairing in this system remains an intriguing aspect which has not yet been fully explored.

The comprehensive exploration of superconductivity at the microscopic level in the bulk of $Ir_{1-\delta}Sb$ and optimally doped $Ir_{1-x}Rh_xSb$ ($x = 0.3$) is therefore essential, requiring both experimental and theoretical investigations. In this context, our focus is on muon spin rotation/relaxation/resonance (μSR) measurements of the magnetic penetration depth, λ in these superconductors[15,16]. This parameter is fundamental to understanding superconductivity, as it is directly related to the superfluid density, n_s through the expression, $1/\lambda^2 = \mu_0 e^2 n_s/m^*$ (where m^* is the effective mass). The temperature dependence of λ is particularly sensitive to the structure of the superconducting gap[15,17]. Moreover, zero-field μSR proves to be a powerful tool for detecting a spontaneous magnetic field arising from time-reversal symmetry (TRS) breaking in exotic superconductors[18–21]. This is particularly noteworthy as internal magnetic fields as small as 0.1 G can be detected in measurements without the application of external magnetic fields. These investigations aim to unveil the intricate details of the superconducting state in $Ir_{1-\delta}Sb$ and $Ir_{1-x}Rh_xSb$, and contribute to our broader understanding of unconventional superconductivity in these materials.

We report on the fully gapped and time-reversal invariant superconducting state in the bulk of $Ir_{1-\delta}Sb$ and $Ir_{0.7}Rh_{0.3}Sb$. The fully gapped nature suggests a well-defined energy structure in the superconducting state, while time-reversal invariance emphasizes the preservation of fundamental symmetries in the superconducting order parameter. The zero-temperature limit of the penetration depth was evaluated to be approximately 319(7) nm and 639(10) nm for $Ir_{1-\delta}Sb$ and $Ir_{0.7}Rh_{0.3}Sb$, respectively. The T_c/λ_{eff}^{-2} ratio was found to be comparable to that of unconventional superconductors. The relatively high critical temperature (T_c) despite a small carrier density raises the intriguing possibility of an unconventional pairing mechanism in Ir-Sb binary superconductors. This observation opens avenues for further investigation into the underlying physics of superconductivity in these materials, potentially revealing mechanisms that contribute to their unique superconducting properties.

Results and discussion

The investigation into the possible magnetism, both static and fluctuating, in $Ir_{1-\delta}Sb$ and $Ir_{1-x}Rh_xSb$ with $x = 0.3$ involved zero-field muon spin relaxation (ZF-μSR) experiments conducted both above and below the critical temperature, T_c. Figure 1a and b illustrate that, down to 1.7 K, no evidence of either static or fluctuating magnetism was detected in the ZF time spectra. The ZF-μSR spectra can be well described by the Gaussian Kubo-Toyabe (GKT) depolarization function[22]:

$$A_{ZF}^{GKT}(t) = A_0\left(\frac{1}{3} + \frac{2}{3}\left(1 - \Delta_{ZF}^2 t^2\right)\exp\left[-\frac{\Delta_{ZF}^2 t^2}{2}\right]\right) \quad (1)$$

Here, Δ/γ_μ is the width of the local field distribution due to the presence of the dense system of nuclear moments. $\gamma_\mu = 0.085\ \mu s^{-1}G^{-1}$ is the muon gyromagnetic ratio. The inset of Fig. 1a shows the temperature evolution of Δ, which shows no enhancement across T_c. The initial asymmetry was also found to be temperature independent and remained constant throughout the analysis. The absence of any change in the ZF-μSR relaxation rate across T_c suggests the lack of spontaneous magnetic fields associated with a time-reversal symmetry (TRS) breaking pairing state in $Ir_{1-\delta}Sb$ and $Ir_{1-x}Rh_xSb$ with $x = 0.3$.

Figure 2a, b depicts the TF-μSR time spectra for $Ir_{1-\delta}Sb$ and $Ir_{0.7}Rh_{0.3}Sb$, respectively. These measurements were conducted in an applied magnetic field of 30 mT, both above (4 K) and below (0.08 K) the superconducting transition temperature, T_c. The measurements for $Ir_{0.7}Rh_{0.3}Sb$ were also conducted under an applied magnetic field of 10 mT. The data were collected after field-cooling the sample from above T_C. The applied field was selected based on the criterion $B_{c1} < B \ll B_{c2}$. Under this condition, a well-ordered Abrikosov vortex lattice is formed. The zero-temperature limits of B_{c1} and B_{c2} of $Ir_{1-\delta}Sb$ synthesized at 5.5 GPa are determined to be 28 mT and 1.19 T, respectively[13]. Consequently, the calculated Ginzburg-Landau parameter κ is estimated to be $\kappa \simeq 6.2$. For $Ir_{0.7}Rh_{0.3}Sb$, the zero-temperature limits of B_{c1} and B_{c2} are determined to be 8 mT and 0.9 T, respectively[13]. These values confirm the suitability of our applied magnetic field. Above T_c the oscillations show a small relaxation due to the random local fields from the nuclear magnetic moments. At 0.08 K, the relaxation rate increases due to the formation of a flux-line lattice (FLL) in the superconducting state, resulting in a nonuniform local field distribution. It is noteworthy that the rise in relaxation rate in the superconducting state is more pronounced in $Ir_{1-\delta}Sb$ compared to $Ir_{0.7}Rh_{0.3}Sb$. This distinction is further evident in the Fourier transforms (see Fig. 2c, d) of the μSR time spectra, highlighting a significant broadening of the signal in the superconducting state for $Ir_{1-\delta}Sb$, whilst the spectra are almost identical above and below T_c in $Ir_{0.7}Rh_{0.3}Sb$.

As denoted by the solid lines in Fig. 2a, c, TF-μSR data were analyzed using the following functional form[23]:

$$A_{TF_s}(t) = \sum_{i=1}^{2} A_{s,i} e^{\left[-\frac{(\sigma_{sc,i}^2 + \sigma_{nm}^2)t^2}{2}\right]} \cos(\gamma_\mu B_{int,s,i} t + \varphi). \quad (2)$$

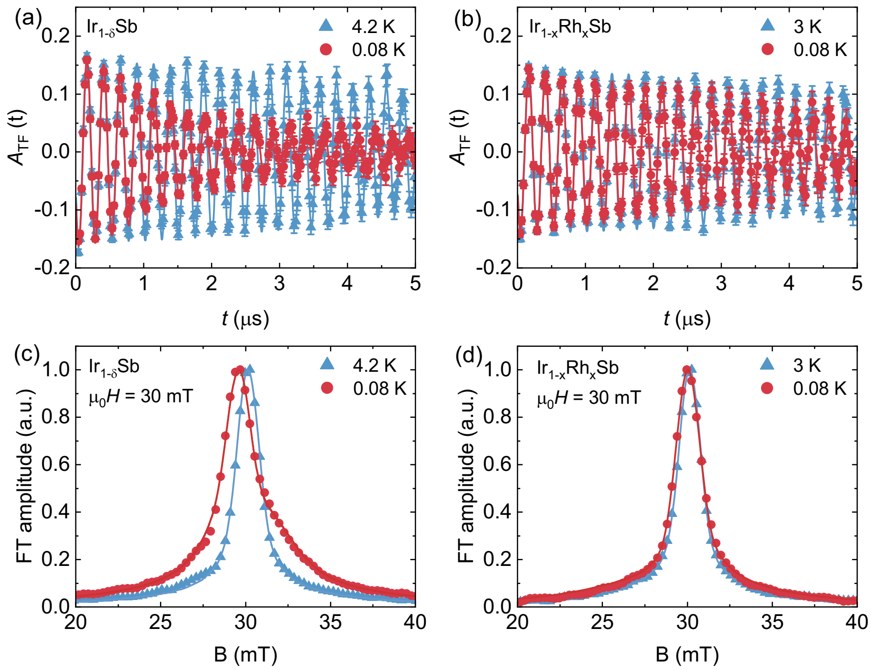

Fig. 2 | Transverse-field (TF) μSR time spectra and the corresponding Fourier transforms. μSR time spectra are obtained above and below T_c in the applied magnetic field of 30 mT (after field cooling the sample from above T_c) for $Ir_{1-\delta}Sb$, synthesized at 5.5 GPa, (**a**) and $Ir_{1-x}Rh_xSb$ with $x = 0.3$ (**b**). The corresponding Fourier transforms are shown in panel **c** for $Ir_{1-\delta}Sb$, synthesized at 5.5 GPa and in panel **d** for $Ir_{1-x}Rh_xSb$ with $x = 0.3$. Error bars are the s.e.m. in about 10^6 events. The error of each bin count n is given by the s.d. of n. The errors of each bin in $A(t)$ are then calculated by s.e. propagation. The solid lines in **a** and **b** represent fits to the data by means of Eq. (2). The solid lines in **c** and **d** are the Fourier transforms of the fitted time spectra.

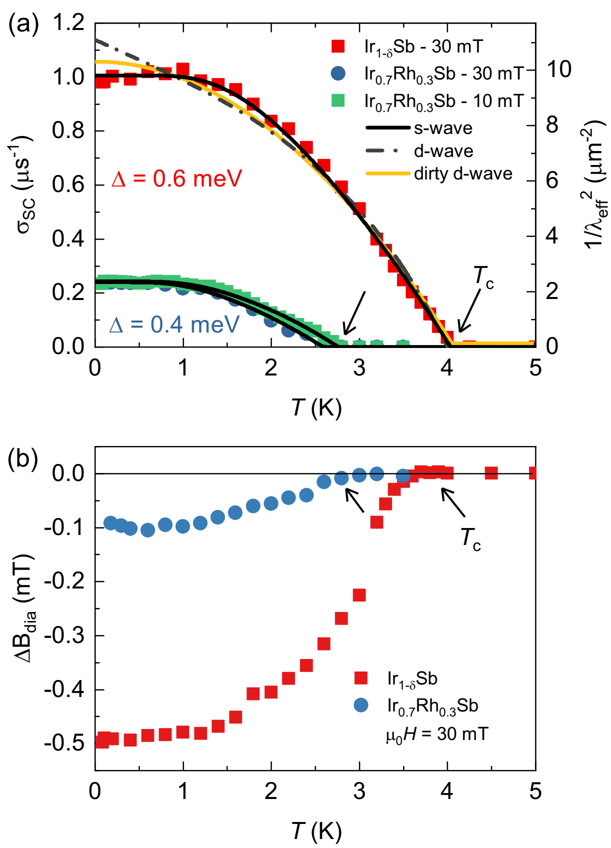

Fig. 3 | Superconducting muon spin depolarization rate σ_{sc} and the field shift. **a** Temperature dependence of the superconducting muon spin depolarization rate, σ_{sc} (left y-axis), and λ_{eff}^{-2} (right y-axis) measured in an applied magnetic fields of $\mu_0H = 10$ mT and 30 mT for $Ir_{1-\delta}Sb$, synthesized at 5.5 GPa and $Ir_{1-x}Rh_xSb$ with $x = 0.3$. **b** Temperature dependence of the difference between the internal field μ_0H_{SC} measured in the SC state and the one measured in the normal state μ_0H_{NS} at $T = 5$ K for $Ir_{1-\delta}Sb$ and $Ir_{1-x}Rh_xSb$. The error bars represent the standard deviation of the fit parameters.

The field distribution in the superconducting state of the sample $Ir_{1-\delta}Sb$ synthesized at 5.5 GPa exhibits a noticeable broadening with an asymmetric line shape, as anticipated in the vortex state (see Fig. 2c). As a result, a two-component expression was utilized to accurately represent this broad and asymmetric field distribution. Conversely, the field distribution for the sample $Ir_{0.7}Rh_{0.3}Sb$ (see Fig. 2d) in the superconducting state displays a significantly narrower width compared to $Ir_{1-\delta}Sb$ and can be adequately represented by a single-component Gaussian. In Eq. (2), $A_{s,i}$, $B_{int,s,i}$ and $\sigma_{sc,i}$ are the the initial asymmetry, the internal magnetic field at the muon site and the superconducting relaxation rates of the i-th component. σ_{nm} characterizes the damping due to the nuclear magnetic dipolar contribution. Since the relaxation rate remains nearly unchanged above T_c upon the application of a magnetic field, this indicates the absence of field-induced magnetism, with only nuclear magnetic moments contributing to the normal state muon depolarization rate. During the analysis σ_{nm} was assumed to be constant over the entire temperature range and was fixed to the value obtained above T_c. In order to extract the superconducting muon spin depolarization rate σ_{sc} (the second moment of the field distribution) and $B_{int,s}$ (the first moment of the field distribution) from the two-component fit we used the same procedure as described in ref. 24.

In Fig. 3a, σ_{sc} is plotted against temperature for both $Ir_{1-\delta}Sb$, synthesized at 5.5 GPa (at $\mu_0H = 0.03$ T), and for $Ir_{0.7}Rh_{0.3}Sb$ (at $\mu_0H = 0.01$ T and 0.03 T). Below T_c, the relaxation rate σ_{sc} begins to increase from zero due to the formation of the flux-line lattice (FLL) and saturates at low temperatures. The temperature dependence of σ_{sc} reflects the topology of the superconducting gap and is consistent with the presence of a single superconducting gap on the Fermi surface of these materials, as we show below. The absolute value of σ_{sc} is five times smaller for $Ir_{0.7}Rh_{0.3}Sb$ compared to $Ir_{1-\delta}Sb$, indicating a lower superfluid density for the Rh-doped sample. Below T_c, a large diamagnetic shift of $B_{int,s}$ experienced by the muons is observed in both samples. In Fig. 3b, the temperature dependence of the diamagnetic shift $\Delta B_{dia} = B_{int,s,SC} - B_{int,s,NS}$ is plotted, where $B_{int,s,SC}$ represents the internal field measured in the superconducting state, and $B_{int,s,NS}$ is the internal field measured in the normal state at 5 K. This diamagnetic shift indicates the bulk nature of superconductivity and rules out the possibility of field-induced magnetism in these superconductors.

To perform a quantitative analysis, it is important to note that the London magnetic penetration depth, $\lambda(T)$ is directly related to the measured

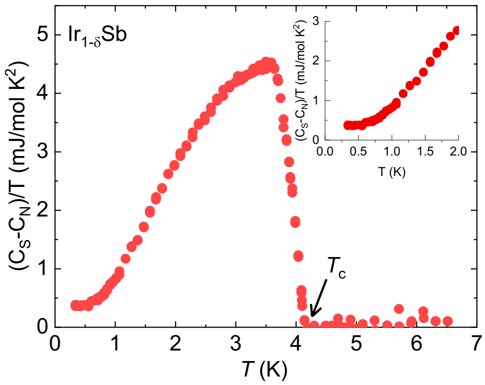

Fig. 4 | Specific heat. Temperature evolution of the electronic part of specific heat for the $Ir_{1-\delta}Sb$, synthesized at 5.5 GPa. The inset shows a zoomed-out version of the low-temperature points, clearly displaying the saturation.

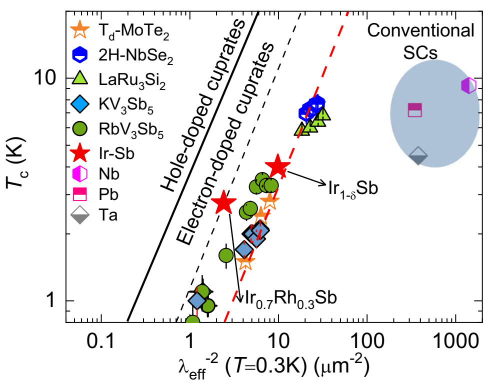

Fig. 5 | Hallmark feature of unconventional superconductivity. Plot of T_c versus $\lambda_{eff}^{-2}(0)$ on a logarithmic scale obtained from μSR experiments for $Ir_{1-\delta}Sb$, synthesized at 5.5 GPa and $Ir_{0.7}Rh_{0.3}Sb$. The data for the kagome-lattice superconductors KV_3Sb_5[20,21,41], RbV_3Sb_5[41], and $LaRu_3Si_2$[46] are also included. The dashed red line represents the relationship obtained for the layered transition metal dichalcogenide superconductors, T_d-$MoTe_2$ and 2H-$NbSe_2$ by Guguchia et al.[39,40]. The relationship observed for cuprates is shown[36,38] as well as the points for various conventional superconductors.

relaxation rate in the superconducting state, σ_{sc}. The triangular FLL relationship is described by the equation[25]:

$$\frac{\sigma_{sc}^2(T)}{\gamma_\mu^2} = 0.00371\frac{\Phi_0^2}{\lambda^4(T)}, \tag{3}$$

where $\Phi_0 = 2.068 \times 10^{-15}$ Wb is the magnetic-flux quantum. Equation (3) is applicable only when the separation between vortices is smaller than λ. In this particular scenario, as per the London model, σ_{sc} becomes field-independent[25].

To explore the superconducting gap structure of $Ir_{1-\delta}Sb$ and $Ir_{0.7}Rh_{0.3}Sb$, we conducted an analysis of the temperature dependence of the magnetic penetration depth, $\lambda(T)$, directly linked to the superconducting gap. The behavior of $\lambda(T)$ can be characterized within the local (London) approximation ($\lambda \gg \xi$) using the following expression[23,26]:

$$\frac{\lambda^{-2}(T,\Delta_{0,i})}{\lambda^{-2}(0,\Delta_{0,i})} = 1 + \frac{1}{\pi}\int_0^{2\pi}\int_{\Delta(T,\varphi)}^{\infty}\left(\frac{\partial f}{\partial E}\right)\frac{EdEd\varphi}{\sqrt{E^2-\Delta_i(T,\varphi)^2}}, \tag{4}$$

where $f = [1+\exp(E/k_BT)]^{-1}$ is the Fermi function, φ is the angle along the Fermi surface, and $\Delta_i(T,\varphi) = \Delta_{0,i}\Gamma(T/T_c)g(\varphi)$ ($\Delta_{0,i}$ is the maximum gap value at $T = 0$). The temperature dependence of the gap is approximated by the expression $\Gamma(T/T_c) = \tanh\{1.82[1.018(T_c/T-1)]^{0.51}\}$[27]. while $g(\varphi)$ describes the angular dependence of the gap and it is replaced by 1 for an s-wave gap, $[1+a\cos(4\varphi)/(1+a)]$ for an anisotropic s-wave gap and $|\cos(2\varphi)|$ for a d-wave gap[28].

In Fig. 3a, the experimentally obtained $\lambda_{eff}^{-2}(T)$ dependence is most accurately described by a momentum-independent s-wave model with a gap value of $\Delta = 0.6(1)$ meV and $T_c = 4.1(1)$ K for $Ir_{1-\delta}Sb$, and a gap value of $\Delta = 0.4(1)$ meV and $T_c = 2.7(2)$K for $Ir_{0.7}Rh_{0.3}Sb$. The d-wave and p-wave gap symmetries were also considered but were found to be inconsistent with the data (illustrated by the dashed line in Fig. 3a). Particularly, these models struggle to account for the very weak temperature dependence of $\lambda(T)$ at low temperatures. We note that the ($p_x + ip_y$) pairing symmetry is also characterized by the full gap in 2D systems and should also saturate at low temperatures. However, the possibility of $p_x + ip_y$ pairing is excluded by the absence of a TRS breaking state. It should also be noted, though, that saturation of the muon depolarization rate at low temperatures can arise even in a nodal d-wave[29–34] superconductor, but in the dirty limit. In this case a power law $\left[1-\left(\frac{T}{T_c}\right)^2\right]$ temperature dependence was proposed theoretically[35]. We tested this function but deemed it inconsistent with the data (see Fig. 3a). Therefore, our analysis shows that a nodeless or fully gapped state is the most plausible bulk superconducting pairing state for $Ir_{1-\delta}Sb$ and $Ir_{0.7}Rh_{0.3}Sb$. Our specific heat results down to 300 mK for $Ir_{1-\delta}Sb$, synthesized at 5.5 GPa (see Fig. 4), measured on the same sample used for muon spin rotation experiments, show saturation at low temperatures and a large jump at T_c, providing the confirmation for bulk nodeless superconductivity.

The estimated ratio of the superconducting gap to T_c, ($2\Delta/k_BT_c$), is approximately 3.4, aligning with the BCS (Bardeen-Cooper-Schrieffer) expectation[15]. However, it's crucial to acknowledge that a similar ratio can also be anticipated within a Bose-Einstein Condensation (BEC)-like framework. Importantly, the ratio $2\Delta/k_BT_c$, on its own, does not effectively distinguish between BCS or BEC condensation scenarios. Further insights are required to differentiate between these two possibilities and elucidate the nature of the superconducting state in the studied materials. What distinguishes between BCS and BEC superconductivity is a key parameter: the ratio of the superconducting critical temperature to the superfluid density. This ratio, T_c/n_s, plays a crucial role in characterizing the nature of the superconducting state in different materials. In a simplified interpretation of the BEC to BCS crossover, the T_c/n_s ratio serves as a critical parameter. Systems characterized by a small T_c/n_s (with a large superfluid density, n_s) are often considered to reside on the "BCS" side of the crossover. Conversely, systems with a large T_c/n_s (exhibiting a small superfluid density, n_s) are expected to be on the BEC side. Moreover, the correlation between T_c and the superfluid density is anticipated to be significant primarily on the BEC side of the crossover. As one moves from the BCS limit to the BEC limit in the crossover, the nature of the pairing mechanism evolves, transitioning from Cooper pairs formed through electron-phonon interactions (BCS) to a more Bose-Einstein condensation-like scenario involving preformed pairs.

The observation of a correlation between T_c and the superfluid density (λ_{eff}^{-2}) was first noted in hole-doped cuprates back in 1988–89[36,37], extending later to include electron-doped cuprates[38]. This intriguing relationship has been investigated across various superconducting systems. Guguchia and collaborators demonstrated that this linear correlation is an intrinsic feature in superconductors such as transition metal dichalcogenides[15,39] and kagome-lattice superconductors[20,40,41]. The ratio T_c/λ_{eff}^{-2} in these systems tends to be lower than that observed in hole-doped cuprates (see Fig. 5). To contextualize the superconductors $Ir_{1-\delta}Sb$ and $Ir_{0.7}Rh_{0.3}Sb$ within this framework, Fig. 5 illustrates the critical temperature plotted against the superfluid density. For $Ir_{0.7}Rh_{0.3}Sb$, the estimated ratio T_c/λ_{eff}^{-2} is approximately 1 ($K/\mu m^{-2}$), closely resembling electron-doped cuprates known for their correlated superconductivity. In the case of $Ir_{1-\delta}Sb$, the ratio is reduced to 0.4 ($K/\mu m^{-2}$) but remains notably distant from conventional BCS superconductors. Intriguingly, it aligns nearly perfectly with the trend line

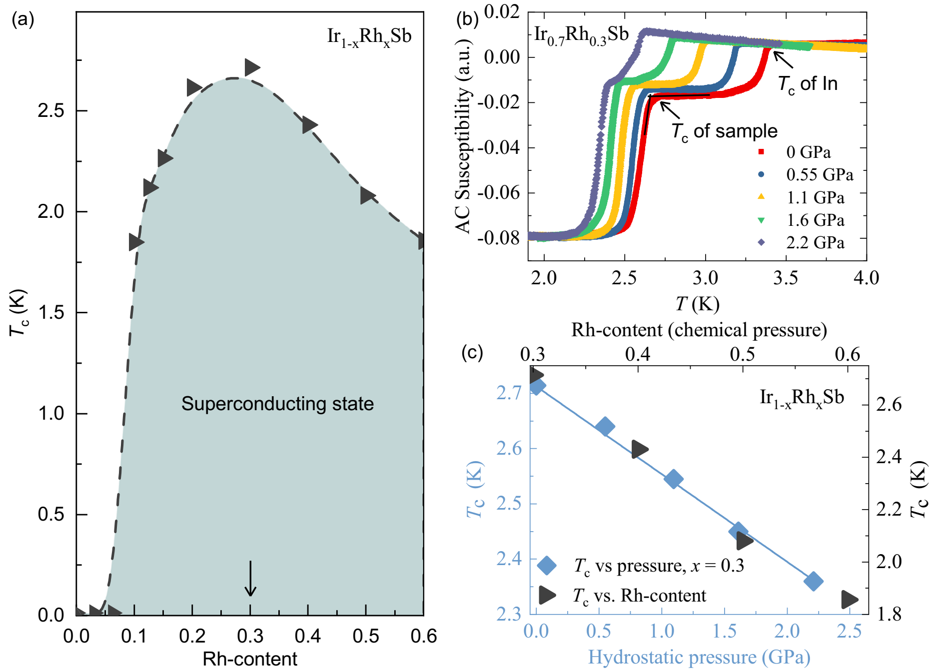

Fig. 6 | Chemical and hydrostatic pressure effects on superconductivity in $Ir_{1-x}Rh_xSb$. a The superconducting critical temperature vs Rh-content, showing a dome-shaped SC phase diagram (adapted from ref. 13). The arrow indicates the sample with $x = 0.3$, which was measured under hydrostatic pressure. **b** The temperature dependence of AC susceptibility, measured at various hydrostatic pressures, ranging up to 2.21 GPa. **c** The superconducting critical temperature as a function of hydrostatic pressure and the Rh-content ("chemical pressure") in the range between $x = 0.3$ and 0.6. The intention of this figure is to qualitatively illustrate the linear suppression of T_c both by hydrostatic pressure and Rh-content.

occupied by charge density wave superconductors like 2H-$NbSe_2$, 4H-$NbSe_2$, $LaRu_3Si_2$, as well as the Weyl-superconductor T_d-$MoTe_2$[15]. This finding strongly suggests an unconventional pairing mechanism in $Ir_{1-\delta}Sb$ and $Ir_{0.7}Rh_{0.3}Sb$, characterized by a low density of Cooper pairs. It is beyond the scope of this work to comment on the microscopic origin of the similarity between Ir-Sb and other superconductors.

Another unconventional feature in the superconducting phase diagram of $Ir_{1-x}Rh_xSb$ is a dome-shaped dependence of T_c (see Fig. 6a). This pattern is characterized by an optimal T_c value occurring at $x = 0.3$, followed by a reduction as the Rh concentration deviates from this optimal point. The isovalent Rh substitution on the Ir site in IrSb, without introducing additional holes or electrons, creates a condition often termed "chemical pressure". Typically, chemical substitution introduces disorder effects, potentially influencing T_c. To discern the intrinsic nature of this dome shape, a cleaner external parameter is essential. For example, hydrostatic pressure introduces fewer disorder effects compared to isovalent chemical substitutions ("chemical pressure"). For this reason, we explored the impact on T_c in the optimally Rh-doped, $Ir_{0.7}Rh_{0.3}Sb$ with hydrostatic pressure, spanning a range up to $p = 2.2$ GPa. As shown in Fig. 6b, c, the observed trend revealed a linear decrease in T_c with increasing pressure. This behavior qualitatively mirrors the effect of Rh doping. The figure is intended to illustrate the linear suppression of T_c by both hydrostatic pressure and Rh content. In the manuscript, we do not provide a quantitative relationship between hydrostatic pressure and the chemical pressure induced by Rh content. Our main point is that this finding suggests the impact of both external hydrostatic pressure and chemical modifications is consistent in the $Ir_{0.7}Rh_{0.3}Sb$ system. This underscores that the reduction in T_c beyond $x = 0.3$, resulting in a dome-shaped dependence, is primarily due to chemical pressure rather than disorder.

Conclusions

In summary, our study provides a microscopic exploration of superconductivity in $Ir_{1-\delta}Sb$ (synthesized at 5.5 GPa with $T_c = 4.2$ K) and optimally Rh-doped $Ir_{0.7}Rh_{0.3}Sb$ ($T_c = 2.7$ K) in close proximity to vacancy ordering, employing a bulk sensitive local probe. Specifically, we investigated the zero-temperature magnetic penetration depth $\lambda_{eff}(0)$ and the temperature dependence of λ_{eff}^{-2} through μSR experiments. The superfluid density in both systems aligns with a scenario of a complete gap. Intriguingly, the T_c/λ_{eff}^{-2} ratio is comparable to that of high-temperature unconventional superconductors, suggesting the unconventional nature of superconductivity in Ir-Sb binary superconductors. Additionally, the μSR experiments, serving as an extremely sensitive magnetic probe, do not exhibit evidence of spontaneous magnetic fields, which would be expected for a time-reversal-symmetry-breaking state in the bulk of the superconductor. Consequently, our results categorize $Ir_{1-\delta}Sb$ and $Ir_{0.7}Rh_{0.3}Sb$ as unconventional, time-reversal-invariant, and fully gapped bulk superconductors. We further demonstrate the similarity between the effects of chemical pressure, induced by isovalent Rh substitution, and hydrostatic pressure on the superconducting critical temperature in $Ir_{0.7}Rh_{0.3}Sb$. This highlights that the observed dome-shaped dependence of T_c is not merely a consequence of disorder effects introduced by chemical substitution but is rooted in the intrinsic properties of the material. These results offer valuable insights into the underlying mechanisms governing the materials behavior. A more comprehensive analysis requires consideration of various factors, including the specific pairing mechanisms and the role of interactions in the superconducting state.

Methods

Sample growth and characterization

The details of the synthesis of the polycrystalline samples of $Ir_{1-\delta}Sb$ and $Ir_{0.7}Rh_{0.3}Sb$ are reported elsewhere[13,14].

Sample characterization

A comprehensive characterization of the δ parameter was conducted in our previous publication[13]. Using an electron probe microanalyzer (EPMA), we determined the Ir deficiency in the $Ir_{1-\delta}Sb$ series, observing that the filling rate increased gradually with higher synthesis pressure. At 5.5 GPa, the δ was approximately 4%. The characterization of the basic physical properties (magnetic susceptibility, electrical resistivity, and heat capacity) for $Ir_{1-\delta}Sb$ at various synthesized external pressures and $Ir_{1-x}Rh_xSb$ samples is also detailed in the same publication[13]. Samples from the same batch were used in the current investigation.

Experimental details

Zero field (ZF) and transverse field (TF) μSR experiments were performed on the GPS (πM3 beamline)[42], and high-field HAL-9500 instruments (πE3 beamline)[43], equipped with BlueFors vacuum-loaded cryogen-free dilution refrigerator (DR), at the Swiss Muon Source (SμS) at the Paul Scherrer

Institute, in Villigen, Switzerland. Zero field is dynamically obtained (compensation better than 30 mG) by a newly installed automatic compensation device[42]. When performing measurements in zero-field the geomagnetic field or any stray fields are tabulated and automatically compensated by the automatic compensation device. The μSR time spectra were analyzed using the free software package MUSRFIT[23]. AC susceptibility experiments under pressure were carried out using double wall piston-cylinder type of cell made of MP35N/MP35N material generate pressures up to 2.3 GPa[40,44,45]. A small indium plate was placed together with the sample in the pressure cell filled with the Daphne oil. The pressure was estimated by tracking the SC transition of a indium plate by AC susceptibility.

Data availability

All relevant data are available from the authors. Alternatively, the data can be accessed through the data base at the following link http://musruser.psi.ch/cgi-bin/SearchDB.cgiusing the following details: 1. Area: HAL. Year: 2020. Run from 0107 to 0198 and from from 0294 to 0356. 2. Area: GPS. Year: 2020. Run from 0014 to 0037. Year: 2024. Run from 2004 to 2008.

Received: 8 February 2024; Accepted: 29 October 2024;
Published online: 08 November 2024

References

1. Ataca, C. et al. Mechanical and Electronic Properties of MoS_2 Nanoribbons and Their Defects. *J. Phys. Chem. C.* **115**, 3934–3941 (2011).
2. Luo, Y. et al. Defect Engineering of Nanomaterials for Catalysis. *Nanomaterials* **13**, 1116 (2023).
3. Guguchia, Z. et al. Magnetism in Semiconducting Molybdenum Dichalcogenides. *Sci. Adv.* **4**, eaat3672 (2018).
4. Tongay, S. et al. Magnetic properties of MoS_2: Existence of ferromagnetism. *Appl. Phys. Lett.* **101**, 123105 (2012).
5. Wang, Q. H. et al. The Magnetic Genome of Two-Dimensional van der Waals Materials. *ACS Nano* **16**, 6960–7079 (2022).
6. Fang, Y. et al. Fe-vacancy ordering in superconducting $K_{1-x}Fe_{2-y}Se_2$: first-principles calculations and Monte Carlo simulations. *Supercond. Sci. Technol.* **28**, 095004 (2015).
7. Zhang, A. M. et al. Vacancy ordering and phonon spectrum of the iron-based superconductor $K_{0.8}Fe_{1.6}Se_2$. *Phys. Rev. B* **85**, 024518 (2012).
8. Chen, T. K. et al. Fe-vacancy order and superconductivity in tetragonal β-$Fe_{1-x}Se$. *PNAS* **111**, 63–68 (2014).
9. Kazakov, S. M. et al. Uniform patterns of Fe-vacancy ordering in the $K_x(Fe,Co)_{2-y}Se_2$ superconductors. *Chem. Mater.* **23**, 4311–4316 (2011).
10. Ourmazd, A. & Spence, J. C. H. Detection of oxygen ordering in superconducting cuprates. *Nature* **329**, 425–427 (1987).
11. Zimmermann, M. V. et al. Oxygen-ordering superstructures in underdoped $YBa_2Cu_3O_{6+x}$ studied by hard x-ray diffraction. *Phys. Rev. B* **68**, 104515 (2003).
12. Li, Y., Du, S., Weng, Z.-Y. & Liu, Z. In-plane ordering of oxygen vacancies in a high-T_c cuprate superconductor with compressed Cu-O octahedrons: An automated cluster expansion study. *Phys. Rev. Mater.* **4**, 044801 (2020).
13. Qi, Y. et al. Superconductivity from buckled-honeycomb-vacancy ordering. *Sci. Bull.* **66**, 327–331 (2021).
14. Ying, T. et al. Fermi surface nesting, vacancy ordering and the emergence of superconductivity in IrSb compounds. arXiv, https://arxiv.org/abs/2108.13704 (2021).
15. Guguchia, Z. et al. Signatures of the topological s^{+-} superconducting order parameter in the type-II Weyl semimetal T_d-$MoTe_2$. *Nat. Commun.* **8**, 1082 (2017).
16. Sonier, J. E., Brewer, J. H. & Kiefl, R. F. μSR studies of the vortex state in type-II superconductors. *Rev. Modern Phys.* **72**, 769 (2000).
17. Das, D. et al. Unconventional Pressure Dependence of the Superfluid Density in the Nodeless Topological Superconductor α-$PdBi_2$. *Phys. Rev. Lett.* **127**, 217002 (2021).
18. Luke, G. M. et al. Time-reversal symmetry-breaking superconductivity in Sr_2RuO_4. *Nature* **394**, 559 (1998).
19. Hillier, A. D., Jorge, Q. & Cywinski, R. Evidence for Time-Reversal Symmetry Breaking in the Noncentrosymmetric Superconductor $LaNiC_2$. *Phys. Rev. Lett.* **102**, 117007 (2009).
20. Guguchia, Z., Khasanov, R. & Luetkens, H. Unconventional charge order and superconductivity in kagome-lattice systems as seen by muon-spin rotation. *npj Quantum Mater.* **8**, 41 (2023).
21. Mielke III, C. et al. Time-reversal symmetry-breaking charge order in a kagome superconductor. *Nature* **602**, 245–250 (2022).
22. Kubo, R. & Toyabe, T. In Magnetic Resonance and Relaxation, 810; T. Toyabe, M.S. thesis (University of Tokyo, 1966).
23. The fitting of Eq. 4 was performed using the additional library BMW developped by B. Wojek. *Phys. Proc.* **30**, 69 (2012).
24. Khasanov, R. et al. Experimental Evidence for Two Gaps in the High Temperature $La_{1.83}Sr_{0.17}CuO_4$ Superconductor. *Phys. Rev. Lett.* **98**, 057007 (2007).
25. Brandt, E. H. Flux distribution and penetration depth measured by muon spin rotation in high-T_c superconductors. *Phys. Rev. B* **37**, 2349 (1988).
26. Tinkham, M. *Introduction to Superconductivity* (Krieger Publishing Company, 1975).
27. Carrington, A. & Manzano, F. Magnetic penetration depth of MgB_2. *Physica C* **385**, 205 (2003).
28. Fang, M. H. et al. Superconductivity close to magnetic instability in $Fe(Se_{1-x}Te_x)_{0.82}$. *Phys. Rev. B* **78**, 224503 (2008).
29. Khasanov, R. et al. Correlation between oxygen isotope effects on transition temperature and magnetic penetration depth in high-temperature superconductors close to optimal doping. *Phys. Rev. B* **74**, 064504 (2006).
30. Sonier, J.E. μSR studies of cuprate superconductors. *J. Phys. Soc. Japan* **85**, 091005 (2016).
31. Luetkens, H. et al. Field and temperature dependence of the superfluid density in $LaFeAsO_{1-x}F_x$ superconductors: a muon spin relaxation study. *Phys. Rev. Lett*. **101**, 097009 (2008).
32. Harshman, D. R. & Fiory, A.T. Concerning the superconducting gap symmetry in $YBa_2Cu_3O_{7-\delta}$, $YBa_2Cu_4O_8$, and $La_{2-x}Sr_xCuO_4$ determined from muon spin rotation in mixed states of crystals and powders. *J. Phys. Condens. Matter* **23**, 315702 (2011).
33. Leng, H. et al. Muon spin rotation study of the topological superconductor $Sr_xBi_2Se_3$. *Phys. Rev. B* **97**, 054503 (2018).
34. Neha, P., Biswas, P. K., Das, T. & Patnaik, S. Time-reversal symmetry breaking in topological superconductor $Sr_{0.1}Bi_2Se_3$. *Phys. Rev. Materials* **3**, 074201 (2019).
35. Hirschfeld, P. J., Putikka, W. O. & Scalapino, D. J. *d*-wave Model for Microwave Response of High-T_c Superconductors. *Phys. Rev. B* **50**, 10250 (1994).
36. Uemura, Y. J. et al. Universal Correlations between T_c and n_s/m^* (Carrier Density over Effective Mass) in High-T_c Cuprate Superconductors. *Phys. Rev. Lett.* **62**, 2317 (1989).
37. Uemura, Y. J. et al. Basic Similarities among Cuprate, Bismuthate, Organic, Chevrel Phase, and Heavy-Fermion Superconductors Shown by Penetration Depth Measurements. *Phys. Rev. Lett.* **66**, 2665 (1991).
38. Shengelaya, A. et al. Muon-Spin-Rotation Measurements of the Penetration Depth of the Infinite-Layer Electron-Doped $Sr_{0.9}La_{0.1}CuO_2$ Cuprate Superconductor. *Phys. Rev. Lett.* **94**, 127001 (2005).
39. von Rohr, F. O. et al. Unconventional Scaling of the Superfluid Density with the Critical Temperature in Transition Metal Dichalcogenides. *Sci. Adv.* **5**, eaav8465 (2019).

40. Guguchia, Z. et al. Direct evidence for the emergence of a pressure induced nodal superconducting gap in the iron-based superconductor $Ba_{0.65}Rb_{0.35}Fe_2As_2$. *Nat. Commun.* **6**, 8863 (2015).
41. Guguchia, Z. et al. Tunable unconventional kagome superconductivity in charge ordered RbV_3Sb_5 and KV_3Sb_5. *Nat. Commun.* **14**, 153 (2023).
42. Amato, A. et al. The new versatile general purpose surface-muon instrument (GPS) based on silicon photomultipliers for μSR measurements on a continuous-wave beam. *Rev. Sci. Instrum.* **88**, 093301 (2017).
43. Sedlak, K., Scheuermann, R., Stoykov, A. & Amato, A. GEANT4 simulation and optimisation of the high-field μSR spectrometer. *Phys. B* **404**, 970–973 (2009).
44. Khasanov, R. et al. High pressure research using muons at the Paul Scherrer Institute. *High. Press. Res.* **36**, 140–166 (2016).
45. Khasanov, R. Perspective on the muon-spin rotation/relaxation under hydrostatic pressure. *J. Appl. Phys.* **132**, 190903 (2022).
46. Mielke III, C. et al. Nodeless kagome superconductivity in $LaRu_3Si_2$. *Phys. Rev. Mat.* **5**, 034803 (2021).

Acknowledgements

The μSR experiments were carried out at the Swiss Muon Source (SμS) Paul Scherrer Insitute, Villigen, Switzerland. Z.G. acknowledges support from the Swiss National Science Foundation (SNSF) through SNSF Starting Grant (No. TMSGI2_211750). Z.G. acknowledges the useful discussions with Dr. Robert Scheuermann. T.Y. would like to acknowledge the National Natural Science Foundation of China (Grant No. 52250308).

Author contributions

Z.G. conceived and supervised the project. Sample Growth: Y.T. and H.H. μSR experiments, data analysis and corresponding discussions: V.S., J.N.G., D.D., C.M.III., S.S.I., R.K., H.L., and Z.G. Specific heat experiments and corresponding discussions: V.S., S.S., M.M., M.B., and Z.G. Figure development and writing of the paper: Z.G., and V.S., with contributions from all authors. All authors discussed the results, interpretation and conclusion.

Competing interests

The authors declare no competing interests.

Additional information

Correspondence and requests for materials should be addressed to Z. Guguchia.

Peer review information *Communications Physics* thanks James Annett and the other, anonymous, reviewer(s) for their contribution to the peer review of this work.